

An investigation on the impact of two vertically aligned drops on a liquid surface

Akash Paul^a, Bahni Ray^b, Kirti Chandra Sahu^c and Gautam Biswas^{a1}

^a*Department of Mechanical Engineering, Indian Institute of Technology Kanpur, Kanpur - 208016, Uttar Pradesh, India*

^b*Department of Mechanical Engineering, Indian Institute of Technology Delhi, Hauz Khas, New Delhi-110 016, India*

^c*Department of Chemical Engineering, Indian Institute of Technology Hyderabad, Sangareddy 502 284, Telangana, India*

Abstract

The dynamics of two vertically coalescing drops and a pool of the same liquid have been investigated using a Coupled Level Set and Volume of Fluid (CLSVOF) method. Such a configuration enables us to study the dynamic interaction of an arbitrary-shaped liquid conglomerate, formed owing to drop-drop coalescence, with a pool. Similar to drop-pool and drop-drop interactions, partial coalescence is observed when a conglomerate interacts with a pool. The presence of the pool below the father drop is found to influence the coalescence characteristic of the two drops. At the same time, the movement of the capillary waves resulting from the interaction of two drops governs the coalescence dynamics of the conglomerate with the pool. As liquid interfaces interact and generate capillary waves at multiple locations, complex trajectories of capillary waves are observed, which play a crucial role in determining the pinch-off characteristics of the satellite during conglomerate-pool interaction. We examine the effect of the ratio of the diameters of the lower/father drop to the upper/mother drop (D_r) on the coalescence dynamics while maintaining the size of the mother drop constant. The variation in the coalescence dynamics due to change in D_r is quantified in terms of the residence time (τ_r), pinch-off time (τ_p) and the satellite diameter to conglomerate diameter ratio (D_s/D_c).

¹gtm@iitk.ac.in

The coalescence dynamics of the conglomerate is then compared with that of an equivalent spherical drop of the same volume and also with that of a drop initialized with the same shape as that of the conglomerate. Finally, the regions of complete and partial coalescence for the conglomerate-pool interactions are demarcated on the Weber number - diameter ratio ($We - D_r$) space.

1. Introduction

Coalescence of a drop on a liquid pool has intrigued researchers for centuries due to its relevance to natural phenomena (Pumphrey et al., 1989; Thomson and Newall, 1886) and industrial applications (Stone et al., 2004; Thoroddsen et al., 2008). The behaviour of a drop interacting with liquid or solid surfaces is highly dependent on the momentum with which it interacts with the surface (Ajaev and Kabov, 2021). A drop impacting a liquid-air interface involves complex physics in addition to a wide range of practical applications. This phenomenon includes the generation of capillary waves that cause satellite droplets to pinch off from the free surface (a phenomenon known as partial coalescence), crater formation (at low impact velocity), and splashing (at high impact velocity).

An impinging drop in a liquid pool either coalesces completely or partially at low impact velocities, while it may cause splashing if the impact velocity is high. In a certain parametric range, the drop may also bounce back. If the momentum is small, the drop may float on a thin layer of the ambient fluid trapped between the drop and the liquid surface for a finite time (residence time) before getting involved in the coalescence process (Deka et al., 2019b; Kirar et al., 2020; Reynolds, 1881). During this time, the trapped air is released, and the droplet sinks into the pool. Researchers have also attempted to estimate the residence time of a drop on a liquid surface when it floats on the free surface due to the air cushion that exists between the drop and the pool (Charles and Mason, 1960; Kirar et al., 2022). Subsequently, a hole is formed in the film, and the drop experiences a partial coalescence. When the drop comes in contact with the liquid surface, the capillary waves are generated at the contact point and prop-

agate up the drop. The capillary pull from the top and the negative horizontal momentum at the neck cause pinch off, and a satellite drop is formed, with a radius less than that of the falling drop (Blanchette and Bigioni, 2006; Chen et al., 2006; Ray et al., 2010). Unlike complete coalescence, a satellite drop pinches off for partial coalescence, producing a cascade of self-similar events that repeat until the final drop completely merges with the liquid pool. This repeated occurrence of the secondary drops from the parent drop is called a coalescence cascade (Thoroddsen and Takehara, 2000). Honey and Kavehpour (2006) observed up to six secondary drops in which the same fraction reduces the drop size in each cycle of partial coalescence. They attributed this primarily to the capillary force at the pinch-off. Gilet et al. (2007a) investigated the ratio between the secondary and primary drops and the role of the capillary waves on partial coalescence criteria. The partial coalescence is a consequence of the competition between the horizontal and vertical collapse rates. The horizontal collapse is always confined to regions lower than the equator of the initial drop. Hence the partial coalescence is ensured (Gilet et al., 2007a). As the impact velocity or size of the primary drop increases, it undergoes complete coalescence, followed by a splashing phenomenon. A few researchers have also investigated the effect of the temperature difference between the drop and pool on the coalescence dynamics and residence time of droplets on liquid surface (Davanlou, 2016; Kirar et al., 2020; Shahriari et al., 2017; Shen et al., 2022; Thirvikraman et al., 2021).

Another common yet fascinating phenomenon is the dynamics of the coalescence of two drops (Gilet et al., 2007b; Yoon et al., 2007). Thoroddsen et al. (2005) studied the coalescence of both equal and unequal-sized pendent and sessile drops and formulated a model to estimate coalescence speed. Similar to drop-pool interactions, complete and partial coalescence can also be observed in two-drop configurations. Thoroddsen et al. (2005) reported two different types of coalescence phenomena: (i) first-stage coalescence where the mother drop after coalescing with the father drop produces a satellite drop by draining some liquid on the father drop, and (ii) second-stage coalescence where the mother

drop, after coalescing with the father drop, although reaches the incipience of pinch-off, the neck expands without the detachment of the satellite drop. The undetached secondary drop then coalesces with the father drop and forms a column structure again and starts the necking which finally leads to the pinch-off of a satellite drop. This is called second-stage coalescence because the satellite is formed after a two-stage coalescence event, the first necking without pinch-off and the second necking that leads to pinch-off. Based on experiments with water and water-glycerin mixture in an air matrix, Zhang et al. (2009) reported that the minimum size ratio of the two drops below which satellite formation inhibits is 1.55. Deka et al. (2019a) numerically investigated the interaction of two unequal-sized drops that provides important insights into the transition from complete to partial coalescence and also elaborately studied the effects of the governing dimensionless parameters on the coalescence dynamics. A similar configuration was investigated by Singh and Saha (2022). Hassanzadeh et al. (2019) numerically investigated the head-on collision of two drops in a vertical channel and studied the resulting oscillations after merging the drops. Irrespective of whether the drop interacts with a pool or another drop, it was found that increasing the viscosity of the liquid slows down the coalescence process (Ray et al., 2010; Thoroddsen et al., 2005). The effect of the physical properties of the fluid and external electric field on the coalescence dynamics of drops have been discussed in great detail in Kavehpour (2015).

In droplet-film interaction, Tang et al. (2016) illustrated that increasing the liquid film thickness below a critical inertial limit shows the non-monotonic transition between bouncing and merging. Tang et al. (2019) investigated the dynamics of the gas layer when a drop bounces after impacting liquid films of various thicknesses at different Weber numbers. Furthermore, different shapes of the interfacial gas layer have been observed for higher film thickness during the approaching and bouncing stages of the drop. Saha et al. (2019) experimentally investigated the evolution and motion of the vortex ring generated during the coalescence of a drop in a pool of the same liquid. They also classified the effects of inertial, capillary and viscous forces in determining the motion of

the vortex ring. In droplet-droplet interaction, collisions may exhibit various outcomes. Qian and Law (1997) identified five regimes (coalescence after minor deformation, bouncing, coalescence after substantial deformation, coalescence followed by separation for near head-on collisions, and coalescence followed by separation for off-centre collisions) while conducting experiments with water and hydrocarbon droplets. They also suggested that coalescence is facilitated when the surrounding medium contains vapour of the interacting liquid masses. Tang et al. (2012) identified distinct outcomes of the head-on collisions of two droplets and discussed the variation of the critical Weber number that separates bouncing and coalescence regimes with the size ratio of the two colliding drops. Sun et al. (2015) numerically investigated the collision dynamics and internal mixing of droplets of non-Newtonian fluids. They simulated droplet collisions for different combinations of shear-thickening and shear-thinning properties and identified the outcomes in coalescence and mixing dynamics.

Droplet-based microfluidic devices have become increasingly popular in recent years and are employed in many different biochemical and molecular biological tests (Anna, 2016; Barea et al., 2019). Moreover, the collision of droplets is also relevant in atomization and spray combustion processes (Cong et al., 2020). A microscopic liquid bridge forms when two liquid drops come in contact and quickly spreads as the two drops coalesce to form one. The coalescence of two or more drops with another interface is another circumstance that frequently occurs in many applications. Paulsen et al. (2014) examined the effect of the viscosity of the outer fluid on the coalescence dynamics of the two drops. Sprittles and Shikhmurzaev (2012) numerically investigated the coalescence of two identical liquid drops using different models and compared them with the experiments. They found that the interface formation model provides a more accurate description of the natural coalescence process. Chan et al. (2011) reviewed different experimental studies on the interaction and coalescence of deformable drops and bubbles and provided detailed quantitative information on the spatial and temporal evolution of interfacial deformations. Damak and Varanasi (2018) experimentally studied the interaction and agglomeration of

two droplets on a superhydrophobic surface. They identified inertial-capillary and viscous regimes and described both the expansion and retraction phases, and established generalised models to characterise the distinct phenomena observed in their experiments. It was observed that the influence of various drop sizes produces drastically different behaviours while impacting a surface (Liu et al., 2021). They found that the Kelvin-Helmholtz instability promotes splash and that the quantity of splash depends on how much energy is lost before the liquid takes off. He et al. (2021) investigated the impact of a drop on an ultra-thin film and found that the drop exhibits contact bouncing behaviour at the same impact velocity for both low and high film thicknesses. It displays a range of behaviours for intermediate film thickness and when the impact velocity is varied. They presented a phase diagram based on these observations. Despite the significance in practical applications, only a few researchers have examined the effects of multiple droplets (organised in parallel or in a line) on surfaces (Benther et al., 2021; Markt Jr et al., 2021; Poureslami et al., 2023). Recently, Poureslami et al. (2023) investigated the effect of simultaneous double droplets on a pool of molten phase change material (PCM), which results in the droplets evaporating and the PCM solidifying. Benther et al. (2021) considered the dynamics of multiple droplets in different configurations, such as two droplets falling in-line and side-by-side, train of droplets, spray of droplets, etc.

As the above-mentioned review indicates, although the drop-pool and drop-drop interactions have been studied extensively, to the best of our knowledge, the paradigm where these two processes occur subsequently or concurrently has not been investigated yet, which has many consequences in practical applications, such as ink-jet printing and electronic cooling (Stone et al., 2004; Thoroddsen et al., 2008). Therefore, in the present study, we intend to understand the complex phenomenon of the interactions between a conglomerate formed by two coalescing drops and a pool of the same liquid. We examine the impact of the ratio of the diameter of the father (D_f) to mother (D_m) drops and the Weber number (We) on the coalescence dynamics of the conglomeration of two drops of different sizes in a liquid pool while maintaining the size of the mother drop

fixed. Our study provides an insightful interpretation of the physical processes involved during the impact of two vertically aligned drops on a liquid surface and attempts to provide with meaningful explanations for the observed behaviour.

The rest of the paper is organized as follows. The problem is formulated in §2, the numerical method and validation of the present solver are discussed in §3. The results are presented in §4 and concluding remarks are summarized in §5.

2. Formulation

We perform numerical simulations to investigate the coalescence dynamics of conglomerated drops in a liquid pool using a Coupled Level Set and Volume of Fluid (CLSVOF) method. The schematic diagram of the computational domain is shown in figure 1. An axisymmetric cylindrical coordinate system (r, z) with its origin at the centre of the bottom wall (as shown in figure 1) is incorporated in our numerical simulations. Both the drops are initialized in a vertically in-line configuration above the pool. The separation distances between the two drops (Δh_1), and the father drop and pool (Δh_2) are kept very small ($\mathcal{O}(0.01D_m)$), and $\Delta h_2/\Delta h_1 = 1.75$ (unless explicitly mentioned). The positioning of the drops and the pool is done in such a way that the mother and father drops begin coalescing with one another before the conglomerate interacts with the pool. A small initial velocity ($\approx 0.05 \text{ ms}^{-1}$) is imposed on the mother drop for the cases with $We = 0.11$. The father drop is initialized at rest. The drops and the pool are of the same fluid (*fluid 1*), and they coalesce in the surrounding medium (*fluid 2*). Depending on the diameter ratio of the father and mother drops (D_f/D_m), the width (W) and height of the domain (H) are varied in the ranges $3D_m$ to $9D_m$ and $6D_m$ to $18D_m$, respectively.

2.1. Governing equations

The conservation equations for mass and momentum for incompressible Newtonian fluids are given by

$$\nabla \cdot U = 0, \tag{1}$$

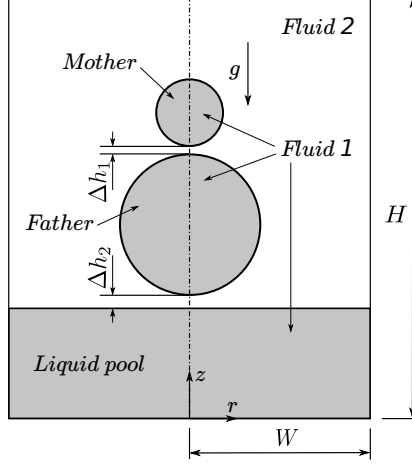


Figure 1: Schematic diagram of the computational domain.

$$\rho(\phi) \left(\frac{\partial \mathbf{U}}{\partial t} + \mathbf{U} \cdot \nabla \mathbf{U} \right) = -\nabla P + \nabla \cdot [\mu(\phi)(\nabla \mathbf{U} + \nabla \mathbf{U}^T)] + \sigma \kappa \mathbf{n} \delta_s + \rho(\phi) \mathbf{g}. \quad (2)$$

Here, $\mathbf{U} = (u, v)$ is the velocity vector having u and v as the radial and axial components of velocity, respectively. P denotes the pressure field, \mathbf{g} is the gravitational field, σ represents surface tension, κ is the mean curvature of the interface, \mathbf{n} is the unit normal vector on the interface boundary, and δ_s is the interface delta function which is zero elsewhere except on the interface. In Eq. (2), the surface tension force is included as a body force term using the formulation proposed by Brackbill et al. (1992). The smoothness of the interface is attained using a level set function ϕ , which is expressed as the signed distance from the interface as

$$\phi = \begin{cases} -d, & \text{in the fluid 2 region,} \\ 0, & \text{at the interface,} \\ +d, & \text{in the fluid 1 region.} \end{cases} \quad (3)$$

The interfacial dynamics is computed by solving the advection equations for the volume fraction F and level set function ϕ , which are given by

$$\frac{\partial F}{\partial t} + \mathbf{U} \cdot \nabla F = 0, \quad (4)$$

$$\frac{\partial \phi}{\partial t} + \mathbf{U} \cdot \nabla \phi = 0. \quad (5)$$

The normal and the curvature are calculated from the level set function ϕ as

$$\mathbf{n} = \frac{\nabla \phi}{|\nabla \phi|}, \quad (6)$$

$$\kappa = -\nabla \cdot \mathbf{n} = -\nabla \cdot \frac{\nabla \phi}{|\nabla \phi|}. \quad (7)$$

A smoothed Heaviside function is defined based on the level set function as

$$F = H(\phi) = \begin{cases} 1, & \text{if } \phi > \delta, \\ \frac{1}{2} + \frac{\phi}{2\delta} + \frac{1}{2\pi} \left[\sin\left(\frac{\pi\phi}{\delta}\right) \right], & \text{if } \phi \leq \delta, \\ 0, & \text{if } \phi < -\delta. \end{cases} \quad (8)$$

Here, δ is the numerical thickness of the interface. It is the distance over which the phase properties are interpolated. The density, $\rho(\phi)$, and the dynamic viscosity, $\mu(\phi)$, of the medium are calculated using the smoothed Heaviside function as

$$\rho(\phi) = \rho_1 H(\phi) + \rho_2 (1 - H(\phi)), \quad (9)$$

$$\mu(\phi) = \mu_1 H(\phi) + \mu_2 (1 - H(\phi)). \quad (10)$$

Next, we discuss the numerical method used in our study.

3. Numerical method

The marker and cell (MAC) algorithm is used to solve the single set of governing equations on a staggered grid arrangement (Harlow and Welch, 1965). In such a grid arrangement, the scalar quantities are defined at the cell centers and the vector quantities, such as the components of the velocity are defined at the center of the cell faces to which they are normal. The governing equations are discretized using the finite-difference method. The grid size in the radial and axial directions is considered to be the same, i.e., $\Delta r = \Delta z$. The discretized momentum equation (Eq. 2) is given by

$$\begin{aligned} U^{n+1} &= U^n + [-\nabla \cdot (U^n U^n)] \Delta t + g \Delta t \\ &+ \left[\frac{-\nabla P^{n+1} + \nabla \cdot 2\mu(\phi^n) \mathbf{D}_v^n + \sigma \kappa(\phi^n) \mathbf{n}(\phi^n)}{\rho(\phi^n)} \right] \Delta t, \end{aligned} \quad (11)$$

where Δt is the time-step and the $D_v = \frac{1}{2}(\nabla U + (\nabla U)^T)$ is the deformation tensor. The convective terms in the momentum equation are discretized using the higher order essentially non-oscillatory (ENO) scheme as described by Chang et al. (1996), and the remaining space derivatives are discretized using the central difference scheme. The discretized form of the momentum equation is solved explicitly for the known volume fraction field F^n , which gives rise to the provisional velocity field. Such a velocity field may not be divergence-free since it does not satisfy the continuity equation in each cell. The compliance of the continuity equation is achieved by solving the corresponding pressure correction equation using the HYPRE multi-grid solver. Thus, after having achieved a divergence-free velocity field, the converged solution is obtained at a new time level. Using this new velocity field, the advection equations of the volume fraction and level set function are solved to obtain the new volume fraction field F^{n+1} and the level set function ϕ^{n+1} , which are essential for interface reconstruction. The second-order conservative operator split advection scheme (Puckett et al., 1997) is used for the discretization of the volume fraction advection equation (Eq. 4). In order to obtain higher accuracy, divergence correction is implemented (Gerlach et al., 2006; Puckett et al., 1997; Rider and Kothe, 1998) Thus, Eq. (4) is reformulated into the conservative form along with the implementation of divergence correction as $\partial F/\partial t + \nabla \cdot (FU) = F\nabla \cdot U$, which is then solved using the operator split advection scheme. The conservation of F is maintained by employing an implicit scheme in the first sweeping direction and an explicit scheme in the second direction as suggested by Puckett et al. (1997). The approach is made second-order accurate by alternating the sweep directions in each time step (Rudman, 1997). The level set advection equation (Eq. 5) is simultaneously solved in the corresponding directions by discretizing the convective terms using the ENO scheme. At each time step, after finding the updated volume fraction F^{n+1} and level set function ϕ^{n+1} , the level set function is reinitialized to the exact signed normal distance from the reconstructed interface by coupling level set function with volume fraction (Son, 2003; Son and Hur, 2002; Sussman and Puckett, 2000). In the present work, the

time-stepping procedure is based on an explicit method to maintain the stability of the solution. During the computations, the time steps are chosen to satisfy Courant-Friedrichs-Lewy (CFL), viscous, and capillary time conditions.

In our simulations, the symmetry boundary condition is used at $r = 0$ and the free-slip boundary condition is employed at the side boundary ($r = W$). The no-slip and no-penetration boundary conditions are used at the bottom wall ($z = 0$), and the Neumann boundary condition is used at the top of the computational domain ($z = H$). Detailed formulation of the boundary condition used here can be found in Deka et al. (2019a); Ray et al. (2010). It is worth mentioning that a noticeable limitation of the current study is the assumption of axisymmetry in the problem. In actual situations, this assumption may not be entirely valid, given that the shape of the conglomerate may not always exhibit symmetry about the vertical axis.

The coalescence behavior of a drop is governed by interfacial tension, gravity, and viscosity of the drop and surrounding fluid. The relevant non-dimensional numbers are the Bond number, $Bo = \rho_c g D_m^2 / \sigma$, Ohnesorge numbers, $Oh_1 = \mu_1 / \sqrt{\rho_a \sigma D_m}$ and $Oh_2 = \mu_2 / \sqrt{\rho_a \sigma D_m}$, Atwood number, $A = \rho_c / 2\rho_a$, Weber number, $We = \rho_1 V_m^2 D_m / \sigma$ and diameter ratio of the father and mother drops, $D_r = D_f / D_m$. Here, ρ_1, ρ_2 are the densities and μ_1, μ_2 are the viscosities of the drop fluid and the matrix fluid, respectively. $\rho_a = (\rho_1 + \rho_2) / 2$ is the average density, $\rho_c = \rho_1 - \rho_2$, is the density difference between the two fluids, and D_m, D_f are the diameters of the mother and father drop, respectively. V_m is the velocity of the mother drop. The length scales are non-dimensionalized using the mother drop diameter D_m and the time is scaled by capillary time $\tau_c = \sqrt{\rho_a D_m^3 / \sigma}$.

3.1. Validation

Our numerical solver is validated by comparing the results obtained from our simulations with the earlier results for (i) the partial coalescence of a drop on a pool of the same liquid and (ii) the partial coalescence of two unequal-sized drops of the same liquid. Additionally, we have also conducted a grid

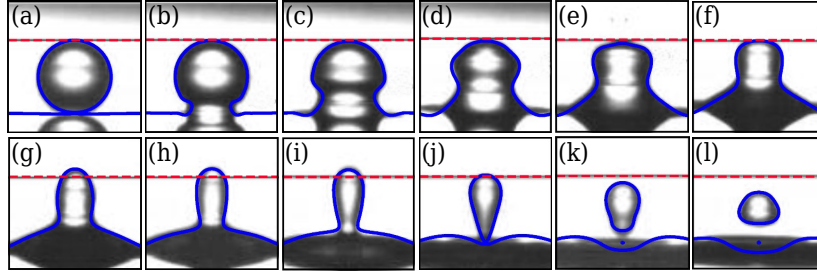


Figure 2: Comparison between the present numerical results (blue line) with the experimental results (in the background) of Chen et al. (2006) for the partial coalescence phenomenon of a drop (diameter 1.1 mm) on a liquid pool. Here, $Oh_1 = 0.0058$, $Oh_2 = 0.0117$, $Bo = 0.0958$ and $A = 0.136$. The panels are $542 \mu\text{s}$ apart in time.

convergence test for the present configuration for a typical set of parameters.

In figure 2, we compare the partial coalescence of a single drop on a liquid pool obtained from our numerical simulation with the experimental result of Chen et al. (2006). The mechanism of partial coalescence is explained in detail in §1. The capillary wave generated at the point of contact propagates upward along the drop surface and imparts an upward vertical pull which elongates the drop beyond its initial height. This can be clearly observed in figure 2(h). The continuous drainage of liquid from the drop and the vertical pull from the capillary waves thins the liquid column. Due to the prevailing horizontal collapse rate, necking starts at the base of the column at a certain point, and a secondary drop pinches off. Figure 2 shows that our numerical results are in good agreement with the experimental results.

Then we validate our solver by simulating the phenomenon of partial coalescence observed during the interaction of two vertically aligned unequal-sized drops of $D_r = 2.72$, which was experimentally investigated by Zhang et al. (2009). It is observed that initially, the upper drop rests on the interface of the lower drop for a finite duration until the film between the two drops ruptures. Due to the breakup of the thin air film between the two drops, some liquid of the mother drop drains out and mixes with the father drop. After some time, it forms a columnar structure that gradually becomes thin and develops

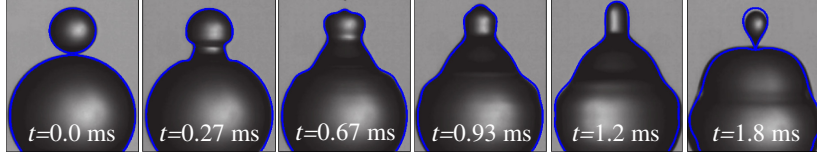


Figure 3: Comparison between the present numerical results (blue line) with the experimental result of Zhang et al. (2009) shown as background for the partial coalescence of two unequal-sized drops with $D_r = 2.72$. The other dimensionless parameters are $Oh_1 = 0.0058$, $Oh_2 = 0.000116$, $Bo = 0.092$ and $A = 0.9976$.

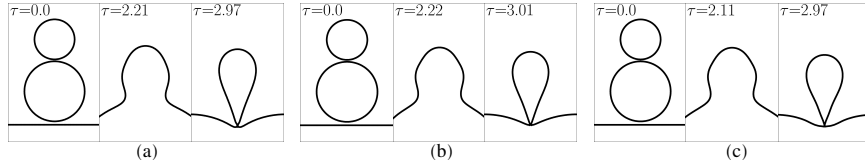


Figure 4: Coalescence dynamics of two unequal-sized drops ($D_r = 1.5$) and a pool obtained using grid sizes (a) $D_m/65$, (b) $D_m/82$ and (c) $D_m/100$. Other dimensionless parameters are $Oh_1 = 0.0058$, $Oh_2 = 0.000116$, $Bo = 0.092$, $A = 0.9976$ and $We = 0.11$.

a neck at its base. Finally, the neck pinches off, generating a daughter drop. Again, the results of our numerical simulations depict a good agreement with the experimental results of Zhang et al. (2009), as illustrated in figure 3.

Further, in order to validate our solver quantitatively, we perform another simulation with $D_f/D_m = 2.87$ and compare our results with that of Zhang et al. (2009). The other dimensionless parameters are $Oh_1 = 0.0082$, $Oh_2 = 0.00006$, $Bo = 0.304$ and $A = 0.9976$. The ratio of the daughter drop diameter to the mother drop diameter in our simulation is found to be 0.545 which is in good agreement with the experimentally observed value of 0.547. This agreement between the numerical and the experimental results justifies the accuracy of the simulations.

3.2. Grid independence

In order to ensure the grid independence, we perform numerical simulations using three grids sizes for the case with $D_r = 1.5$ in the configuration shown in figure 1. The results obtained using the grid sizes $D_m/65$, $D_m/82$ and $D_m/100$

are shown in figure 4(a)-(c). The values of the corresponding dimensionless radius of the resultant satellite drop are 0.526, 0.508 and 0.505, respectively. The percentage difference between the values of radii for grid sizes $D_m/82$ and $D_m/100$ is approximately 0.72 %. Thus, the intermediate grid size of $D_m/82$ has been considered for the rest of the simulations.

4. Results and Discussion

4.1. Coalescence cascade of the conglomerate

The diameter ratio between the father and mother drops (D_r) determines whether the two drops coalesce completely or partially (Deka et al., 2019a; Zhang et al., 2009). For water drops in the surrounding air, with the dimensionless parameters, $Oh_1 = 0.0058$, $Oh_2 = 0.000116$, $Bo = 0.092$ and $A = 0.9976$ (kept fixed in our study), we have performed simulations for different D_r values. Unless mentioned explicitly, throughout the study, $We = 0.11$. The diameter ratio is varied from 1.0 to 3.0, keeping the size of the mother drop constant. This range encompasses the transition from total to partial coalescence for two drops while the interaction of the conglomerate with the liquid pool always produces partial coalescence. Although, at higher We , the conglomerate also shows a transition from total to partial coalescence during its interaction with the pool as the value of D_r is increased.

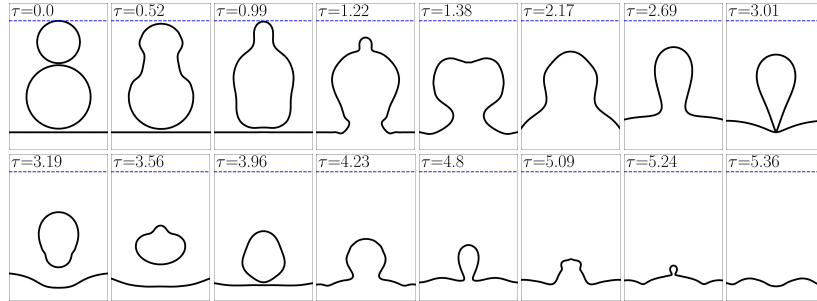


Figure 5: Coalescence dynamics of two unequal-sized drops ($D_r = 1.5$) and a pool for $We = 0.11$. The blue dashed lines represent the initial locations of the tips of the mother drop.

We observe that the two drops merge fully for $D_r \leq 2.25$. For higher D_r values, the mother drop coalesces partially with the father drop and produces a single-stage cascade. For $D_r = 1.5$, the mother drop coalesces completely with the father drop, as shown in figure 5. When the conglomerate is deposited onto the pool, it produces a satellite drop, which eventually coalesces with the pool. Figure 6 shows another situation where the two drops coalesce partially, producing a satellite (daughter) drop. Here, the conglomerate exhibits a two-stage cascade with the pool. Among the D_r values considered here, the conglomerate produces a single-stage cascade with the pool for $D_r = 1, 1.25$ and 1.5 ; while for higher D_r values, it produces a two-stage cascade.

It is to be noted that Tang et al. (2012) observed that the critical Weber number, which separates bouncing and permanent coalescing regimes, does not vary considerably with the diameter ratio of two droplets undergoing head-on collision. In our study, although we did not observe bouncing behavior for vertically aligned drops, we noticed that some conglomerate morphologies bear a striking resemblance to the coalescence regime reported by Tang et al. (2012).

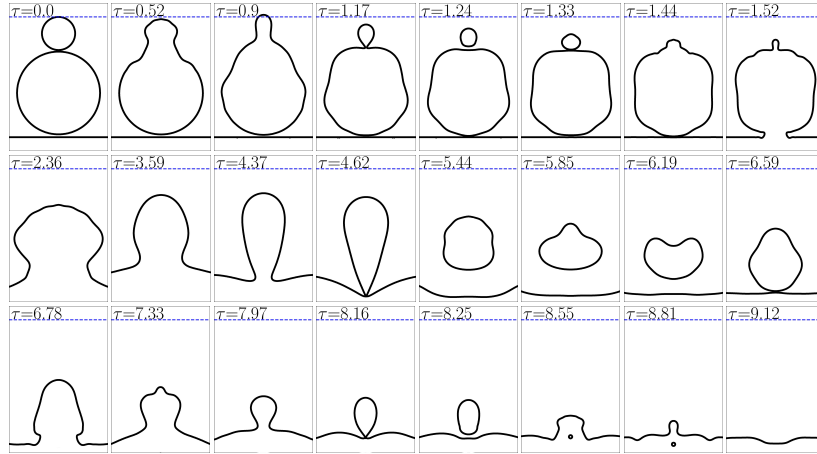


Figure 6: Coalescence cascade for $D_r = 2.5$ and $We = 0.11$.

4.2. Effect of pool on the coalescence dynamics of two drops

In order to estimate the effect of the presence of a pool on the coalescence dynamics of the two drops, we performed a set of simulations for $D_r=2.5$. In this analysis, the value of $\Delta h_2/\Delta h_1$ is suitably adjusted to ensure that the two drops and the father drop and the pool start coalescing simultaneously. We allowed the mother and father drop to coalesce in the absence of pool for one case while for the other two cases, $\Delta h_2/\Delta h_1$ is varied from 0.5 to 0.75. Figure 7(b) and (c) refer to the case where the pool is absent, and it can be seen that a daughter drop is pinched off from the interaction of the mother and father drops. Figure 7(d,e) shows the case for $\Delta h_2/\Delta h_1 = 0.75$. Here, we can see that the daughter drop pinches off in spite of the interaction between the conglomerate and the pool. As we further decrease $\Delta h_2/\Delta h_1$ to 0.5, we can see from figure 7(f,g) that the pinch-off of the daughter drop is prevented due to excessive drainage of the conglomerate into the pool. The vertical collapse rate of the liquid column expedites as a result of this drainage, which also causes the mother drop to start draining more into the father drop (figure 7(f)). It is well known that the competition between the horizontal and vertical rates of collapse leads to partial coalescence. In this scenario, the vertical rate of collapse dominates over the horizontal rate of collapse and partial coalescence is prevented. However, in all these cases it is observed from figure 7(a) that the apex of the mother reaches the same level of height irrespective of the position of the pool.

4.3. Capillary waves

The capillary waves are generated by the interplay between surface tension and the pressure variation in the liquid. These waves, with shorter wavelengths, carry enough momentum to influence the coalescence characteristics of the drops. In the case of a drop interacting with a pool of the same liquid, Blanchette and Bigioni (2006) reported that the partial coalescence depends on the strength of these capillary waves to pull the drop vertically from the top to stretch it. During drop-drop or drop-pool interaction, the capillary waves generated at the interface travel along the interacting fluids. The effect of the

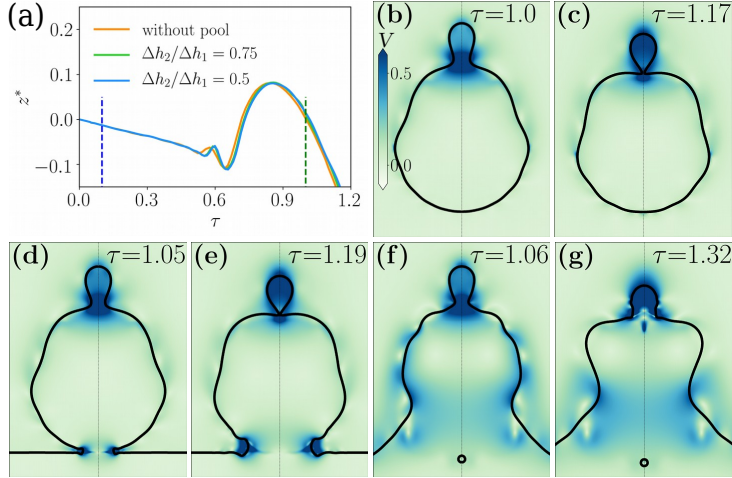


Figure 7: Temporal variation of the dimensionless location of the tip of the mother drop ($z^* = z - z_0/D_m$, z_0 =initial height of the tip of the mother drop) in the presence and absence of the pool. The blue and green vertical dashed lines in (a) denote the instants when the father drop starts draining into the pool for $\Delta h_2/\Delta h_1 = 0.5$ and 0.75 , respectively. The contour represents the resultant velocity (V) for $D_r = 2.5$ and $We = 0.11$. Panels (b) and (c) represent two sequences during father-mother drop interaction when the pool is absent, while panels (d-e) and (f-g) show the sequences when $\Delta h_2/\Delta h_1 = 0.75$ and 0.5 respectively.

capillary waves can be observed profoundly in the vertical stretching of the impinging drop. In figure 6, at $\tau = 0.9$, it can be noticed that the mother drop is elongated beyond the blue dashed line.

In the simple configurations of a drop interacting with a pool or another drop, the coalescence dynamics can be anticipated to a reasonable extent by deciphering the paths of the capillary waves. However, in a complex configuration, such as the one considered in this study, the propagation and interaction of the capillary waves generated at multiple interfaces can influence the coalescence process in unpredictable ways. During the coalescence of a drop on a liquid pool, the capillary waves that travel along the liquid pool do not affect the coalescence dynamics, but in the coalescence of a pair of drops, the capillary waves travelling along the father drop sometimes converge at the bottom and impart a downward pull on the father drop. Also, when the father drop interacts with the pool, another set of capillary waves is generated, some of which start moving

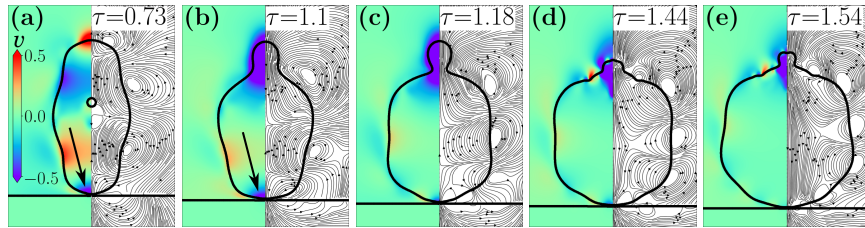


Figure 8: The axial velocity (v) field and streamline pattern at the onset of coalescence of the conglomerate with the pool at $We = 0.11$ for (a) $D_r = 1$ (b) $D_r = 1.5$ (c) $D_r = 2$ (d) $D_r = 2.5$ and (e) $D_r = 3$.

upwards along the periphery of the father drop. The effect of these waves on the coalescence dynamics will be discussed in the context of the interaction of the conglomerate with the pool.

When the two drops coalesce, a conglomerate is formed. In the initial stages, the mother drop contributes to the upper part, while the father drop contributes to the bottom part of the conglomerate. The capillary waves travel in both directions from the location where the mother and father drops interact. The movement of the capillary waves affects the morphology of the conglomerate during coalescence. Figure 8 illustrates the shape of the conglomerate, vertical velocity field and streamline pattern at the onset of coalescence with the pool for different D_r values. As the diameter ratio increases, the capillary waves cease to significantly deform the bottom part of the conglomerate, and it assumes a near-spherical shape till the onset of its coalescence with the pool. For $D_r = 1$, the capillary waves travelling along the periphery of the father drop converge at the bottom of the father drop. This happens before the conglomerate can start coalescing with the pool, and it is evident from the considerable downward momentum in the bottom part of the conglomerate (figure 8(a)). A similar downward momentum can also be seen in figure 8(b) for $D_r = 1.5$. However, with the increase in the size of the father drop, the downward momentum as shown by black arrows in figure 8(a) and (b) gradually vanishes. This result indicates that for small Δh_2 values ($\Delta h_2/\Delta h_1 = 1.75$), the downward momentum developed owing to the converging capillary waves facilitates the coalescence

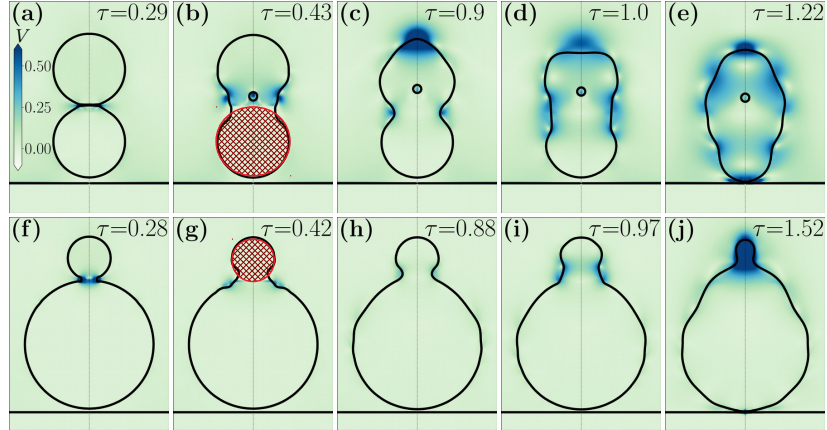


Figure 9: Evolution of the conglomerate during the analysis of the effect of capillary waves by turning the velocity field off for 0.2 ms in the father drop for $D_r = 1$ (a)-(e) and in the mother drop for $D_r = 3$ (f)-(j). The cross-hatched parts in (b) and (g) represent the areas where the velocity is turned off. We value is 0.11.

process. On the other hand, for higher D_r values, the capillary waves travelling along the mother drop converge earlier at the top, imparting an upward pull on the conglomerate and delaying the coalescence process.

To verify the effect of the capillary waves in facilitating/delaying the coalescence of the conglomerates for lower/higher diameter ratios, we perform tests similar to that of Blanchette and Bigioni (2006) and Deka et al. (2019a) by setting the velocity to zero after a particular time instant and restarting the simulation. Here, we interrupt the velocity field for the extreme D_r values in our range. The cross-hatched regions in figure 9(b) and (g) identify the regions where the velocity field is turned off. The upper row (figure 9(a)-(e)) represent the evolution of the conglomerate for $D_r = 1$ while the bottom row (figure 9(f)-(j)) represent the case for $D_r = 3$. We set the velocity to zero in the lower half of the conglomerate for $D_r = 1$, for 0.2 ms at $\tau = 0.43$, and the velocity field distributes naturally after that. By doing this, the effect of the capillary waves in facilitating the coalescence between the conglomerate and the pool is reduced. This is evident from the time instant at which the conglomerate

starts coalescing with the pool, which is delayed ($\tau = 1.22$) compared to the case ($\tau = 0.73$) when the velocity field was not interrupted. A similar study was conducted for $D_r = 3$, where the velocity field was turned off in the upper part of the conglomerate just after the two drops started coalescing with each other. Due to the interruption of the velocity field, the upward pull exerted by the converged capillary waves on the top of the conglomerate is expected to decrease. This indeed advanced the coalescence of the conglomerate with the pool from $\tau = 1.54$ (figure 8(e); original case of uninterrupted velocity field) to $\tau = 1.52$, as shown in figure 9(j). Also, due to the weakening of the upward pull on the top part of the conglomerate, the daughter droplet generation is inhibited in this case.

The time duration for the bottom-most point of the father drop to reach from its initial position to a position at the onset of coalescence of the drop-conglomerate with the pool is defined as residence time. The variation of the dimensionless residence time (τ_r) with D_r is plotted in figure 10(a) and it shows that τ_r increases continuously as D_r is increased. As discussed earlier, the capillary waves travelling along the interface of the father drop in the downward direction would impart a downward pull if converged at the bottom of the conglomerate. At the same time, the capillary waves, moving along the interface of the mother drop, try to pull the drop upwards. With the increasing diameter ratio, the capillary waves travelling downwards along the father drop become ineffective in imparting the downward pull as they cannot travel to the bottom of the conglomerate. On the contrary, due to the increased flatness of the father drop and higher curvature at the point of contact of the two drops, the capillary waves impart a stronger upward pull. This combined effect contributes to an increase in τ_r with the increase in diameter ratio.

Furthermore, increasing D_r increases the dimensionless pinch-off time (τ_p), which can be defined as the time duration from the onset of coalescence to the pinch-off of the first satellite during the conglomerate-pool interaction. This is because, as the size of the father drop increases, the capillary waves require more time to climb to the top of the conglomerate and impart the vertical pull, which

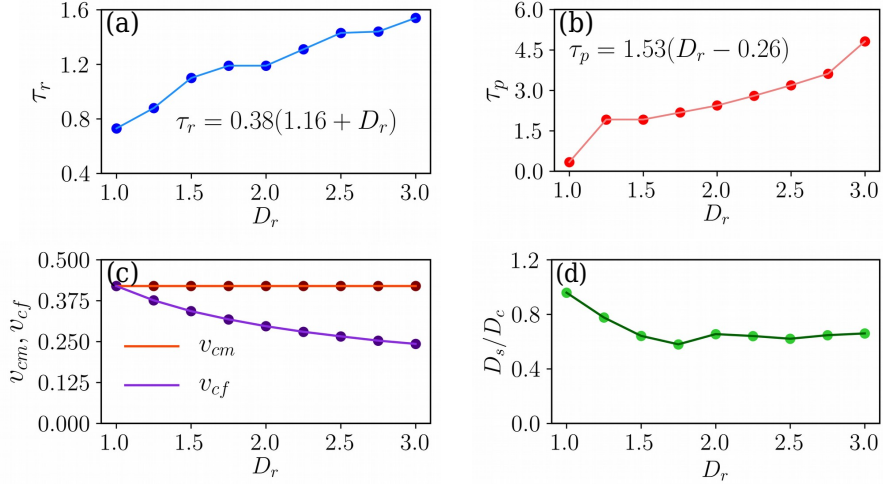


Figure 10: The variations of (a) τ_r (b) τ_p (c) v_{cm} & v_{cf} and (d) D_s/D_c with D_r for $We = 0.11$.

eventually contributes significantly to the pinch-off process. Figure 10(b) shows that increasing D_r increases τ_p . However, in addition to the size, we noticed that the shape of the conglomerate also plays an important role in determining the pinch-off time. In contrast to higher D_r values, the pinch-off time for $D_r = 1$ is quite shorter ($\tau = 0.34$). We observe that the capillary pressure within the drops, the momentum carried by the generated capillary waves, and the local curvature of the neck all along affect the pinch-off dynamics to set the critical limit of pinch-off time. A decrease in the size of the father drop increases the capillary pressure within the father drop, which increases the radial expansion of the neck after coalescence leading to an increase in drainage. Because of the smaller size of the father drop, the curvature in the neck region becomes less sharp. As a result, the capillary waves produced because of the curvature change near the contact region become weaker and carry less momentum. This decreases the vertical stretching of the mother drop and affects the pinch-off dynamics. Moreover, because of less stretching of the mother drop, the local curvature at the neck region increases in the retraction stage of the neck, which also affects the pinch-off dynamics. The rate of the downward pull of the liquid is controlled by the capillary speed of the mother drop, while the capillary speed

of the father drop controls the upward pull. The capillary speeds of the mother drop (v_{cm}) and father drop (v_{cf}) can be defined as

$$v_{cm} = D_m \sqrt{\frac{\sigma}{\rho_a D_m^3}}, \text{ and} \quad (12)$$

$$v_{cf} = D_f \sqrt{\frac{\sigma}{\rho_a D_f^3}}. \quad (13)$$

Figure 10(c) shows the relationship between D_r and the variations of v_{cm} and v_{cf} . The capillary speed of the mother drop, which has a fixed diameter of 0.82 mm, remains constant at 0.42 ms^{-1} . However, the capillary speed of the father drop decreases as D_r increases due to its larger diameter. As depicted in figure 10(c), this decrease in capillary speed causes the capillary waves on the father drop to take longer to converge at the bottom, facilitating coalescence. Our simulation shows that the residence time (τ_r) is related to the diameter ratio as $\tau_r = 0.38(1.16 + D_r)$, and the pinch-off time (τ_p) is related to D_r as $\tau_p = 1.53(D_r - 0.26)$.

Figure 10(d) shows the variation of D_s/D_c with diameter ratio. Here, D_s is the equivalent diameter of the satellite, and D_c is the equivalent diameter of the conglomerate. For $D_r = 1$, it is seen that the satellite drop is of almost the same size as that of the conglomerate ($D_s/D_c = 0.959$), indicating that there is very less drainage in the first stage of coalescence. The ratio gradually decreases with the increase in D_r and finally settles to a nearly constant value. The plausible reasons for the smaller value of τ_p and higher D_s/D_c for smaller values of D_r is explained in detail in the next section.

4.4. Pinch-off dynamics of the conglomerate of equal-sized drops

In figure 11, we have shown the evolution of the conglomerate and the pinch-off of the satellite during the conglomerate-pool interaction for $D_r = 1$. The minimal τ_p value for this case indicates that the pinch-off occurs quite rapidly. The non-columnar shape at pinch-off can be seen in figure 11(d) at $\tau = 1.07$. The shape of the conglomerate in this case resembles a prolate drop. Biswas et al. (2011) studied the effect of drop shape on partial coalescence and reported that

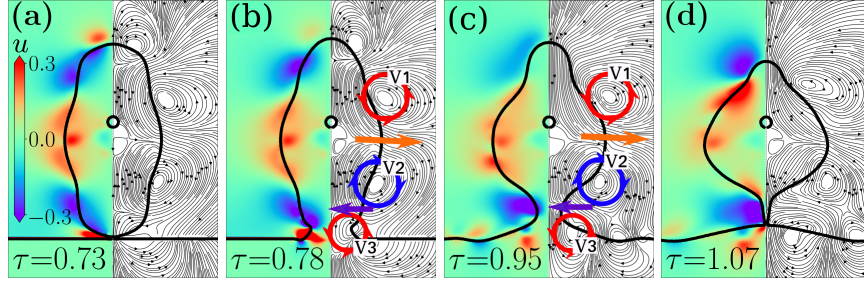


Figure 11: Pinch-off of the satellite during the interaction of the conglomerate with the pool for $D_r = 1$ and $We = 0.11$. The left half and right half of the figure show the radial (u) velocity and the streamlines, respectively.

for the prolate and oblate-shaped drops, the necking and pinch-off phenomena happen faster as compared to a spherical drop. However, in this situation, the effect of shape is complemented by the complex interaction of capillary waves as we will see next. We find that the drop may not always assume a conventional columnar shape during the pinch-off. During the satellite pinch-off, similar shapes (like figure 11(d)) have been observed by Ray et al. (2013) when two drops were allowed to impinge on a pool within a small time interval (10 ms). Yi et al. (2014) had similar observations during the head-on collision of binary droplets on a superhydrophobic surface.

The narrowing of the top and the bottom part of the structure is due to the negative radial (u) velocity, clearly seen in the bluish regions of the contour in figure 11(a-d), while the outward radial bulge in the middle part of the satellite is developed due to the positive u -velocity shown by the reddish region in the middle. The velocity field that engenders this unconventional structure during pinch-off can be attributed to the interplay of the capillary waves generated at multiple liquid-liquid junctions. From the streamlines of figure 11(b) and (c), it can be seen that the capillary waves generated during the interaction of the two drops have an opposite sense of rotation. The waves travelling along the upper and the lower drops rotate in anti-clockwise and clockwise directions and are shown by a red counterclockwise rotating circle (V_1) and blue clockwise ro-

tating circle (V_2), respectively. This pair of capillary waves impart an outward momentum in the central part of the fluid structure, which is shown by the orange arrows. While travelling down the conglomerate, the clockwise rotating capillary wave (V_2) encounters a counterclockwise rotating capillary wave near the neck region (V_3), which is generated at the conglomerate-pool interface. These two capillary waves direct the flow in such a way that it achieves sufficient inward momentum near the neck region to cause an early pinch-off of the satellite.

The early pinch-off effectively stops the conglomerate from draining into the pool, and the resultant satellite retains much of the fluid mass of the conglomerate. Hence, this study clearly explains higher D_s/D_c values associated with the smaller D_r values.

4.5. Comparison with that of a spherical drop

Here, for each diameter ratio, we compare the coalescence dynamics of the conglomerate with that of an equivalent spherical drop of the same volume. Figures 12(a)-(f) illustrate the interface profiles at the onset of coalescence (top) and during satellite pinch-off (bottom) for the conglomerate and the spherical drop for different D_r values. Due to no prior interactions, the spherical drop is devoid of any capillary waves, unlike that of the conglomerate. Figures 12(a) and (b) refer to the case of the conglomerate and the spherical drop respectively. Similarly, figures 12(c) and (d) represent the cases for $D_r = 1.5$ and figures 12(e) and (f) represent the cases for $D_r = 2$.

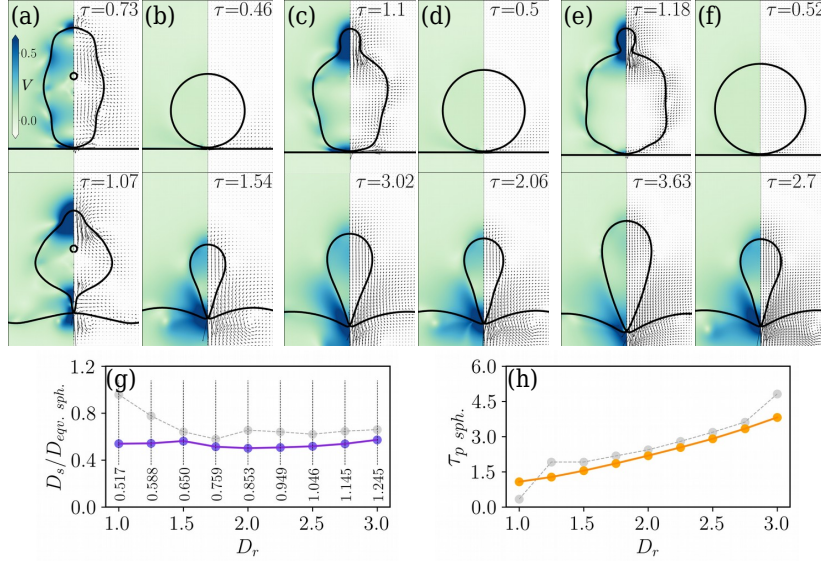


Figure 12: Panels (a) and (b) show the comparison of interface profiles at the onset of coalescence (top) and during pinch-off (bottom) for the conglomerate and the spherical drop respectively, for $D_r = 1$. Similarly, panels (c) and (d) and panels (e) and (f) show the comparison for $D_r = 1.5$ and 2 , respectively. Figure (g) shows the variation of $D_s/D_{equiv. sph.}$ with D_r , while (h) shows the variation of τ_p with D_r for the equivalent spherical drop. The variations of D_s/D_c and τ_p for the conglomerate have been shown using gray dashed curves in the background. The radius of the equivalent spherical drop corresponding to each D_r value is mentioned inside panel (g). We value is 0.11 .

It can be seen that the interface profiles of the conglomerate and the spherical drop vary the most for $D_r = 1$. As D_r increases, the profiles shown in figure 12(c)-(f) indicate that the shape of the conglomerate at the onset of coalescence approaches towards a spherical form as the diameter ratio is increased (more clearly observed in figure 8). Also, the columnar structure during satellite pinch-off for the conglomerate and the spherical drop become almost indistinguishable as we increase D_r .

Figure 12(g) shows the variation of the ratio of the diameter of the satellite (D_s) and the equivalent spherical drop ($D_{equiv. sph.}$) corresponding to each D_r . For higher D_r values, the pinch-off dynamics of the conglomerate and the spherical drop shows qualitatively similar behaviour. However, it is clearly seen that

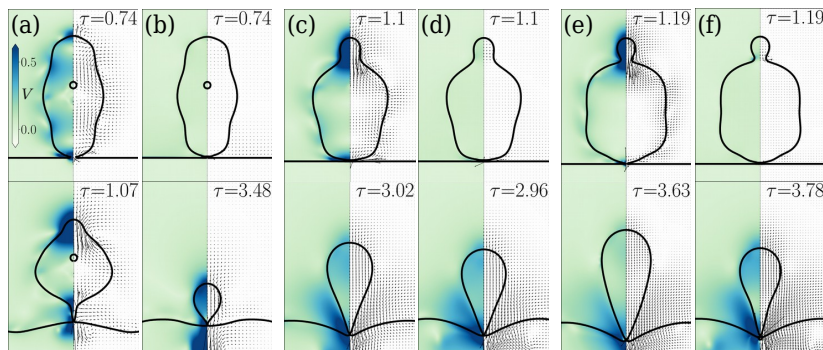


Figure 13: The panels (a), (c) and (e) show the comparison of coalescence dynamics of a conglomerate for $D_r = 1, 1.5$ and 2 respectively. Panels (b), (d) and (f) correspond to a drop initialized with the same shape as that of the conglomerate for $D_r = 1, 1.5$ and 2 , respectively. We value is 0.11 .

for smaller diameter ratios, the size of the satellite produced during the interaction of a purely spherical drop is much smaller than the satellite produced during the conglomerate-pool interaction. For the spherical drop, the $D_s/D_{eqv. sph.}$ ratio remains nearly constant irrespective of the size of the impinging drop, while for the conglomerate, we see that due to the change in the shape of the impinging liquid mass and complex interaction of capillary waves (described in §4.3), the ratio starts-off with a high value and gradually decreases. Here, $\tau_{p sph.}$ is the pinch-off time for the satellite produced during the interaction of the equivalent spherical drop. $\tau_{p sph.}$ increases consistently as D_r is increased unlike that in case of the conglomerate where a sudden jump was observed as D_r was increased from 1 to 1.25 (figure 12(h)). This further demonstrates that as D_r increases, the effect of shape reduces and the coalescence dynamics of the conglomerate approaches that of a pure spherical drop.

4.6. Comparison with a drop with a conglomerate-like initial shape

In §4.5, we have seen that the coalescence of a conglomerate in a pool differs from that of the spherical drop. In this section, we compare the coalescence-dynamics of the conglomerate with a drop of the same shape as that of the conglomerate. This drop can be termed as ‘conglomerate-shaped’ drop. The

conglomerate-shaped drop possesses the shape of the conglomerate but it does not have the presence of the capillary waves generated during the interaction of the father and the mother drop.

Figure 13 compares the instants of the onset of coalescence (top) and pinch-off of the secondary drops (bottom) during the coalescence of the conglomerate and the conglomerate-shaped drop for various diameter ratios. Figures 13(a) and (b) correspond to the cases of conglomerate and the conglomerate-shaped drops respectively, for $D_r = 1$. Similarly, figures 13(c) and (d) and figures 13(e) and (f) correspond to the cases for the conglomerate and the conglomerate-shaped drop for $D_r = 1.5$ and 2 respectively.

For $D_r = 1$, we still do not observe the early pinch-off of the secondary drop which was seen when the conglomerate interacted with the pool, clearly indicating that the capillary waves produced during the drop-drop interaction played a major role for the early pinch-off of the secondary droplet.

When a drop is allowed to impact on a stationary drop placed on a superhydrophobic surface, it is observed that during the retraction phase, the coalesced droplet does not retain any memory owing to its drop-drop interaction and behaves as if it is an isolated primary drop (Damak and Varanasi, 2018). However, in our study, where we employ a similar configuration (the hydrophobic surface being replaced by a pool of the same liquid as that of the drop), the conglomerate is found to retain the memory of its origin in terms of the capillary waves generated during the interaction of the father drop with the mother drop. For smaller D_r values these capillary waves interact with the capillary waves generated during the interaction of the conglomerate and the pool. This facilitates early pinch-off of the secondary droplet (figures 13(a) and (b)). However, for the larger diameter ratios, the capillary waves do not interact and an early pinch-off does not occur. From figures 13(e) and (f), it can be observed that the coalescence-dynamics of the conglomerate and the conglomerate-shaped drop become quite similar.

4.7. Effect of Weber number

With the variation of Weber number (We), we observe different coalescence patterns in drop-drop and conglomerate-pool interactions. In figure 14, we plot the regime map that identifies different coalescence characters of the conglomerates for various D_f/D_m ratio. We observe non-monotonic behavior related to the number of satellite drops with increasing We . In the case of smallest diameter ratio, we observe one satellite formation for $We = 0.03$. While for $We = 0.11$, we observe the formation of two satellites. As we increase the We to 6.37, four satellites are formed. Seemingly, in this range of We , it is a monotonic increase in the number of satellites. The number of satellites reduces to one for $We = 11.32$. Subsequently, for the higher Weber numbers, for example, for $We = 20.02$, the conglomerate coalesces completely without forming any satellite, and $We = 31.56$ repeats the complete coalescence behavior. However, for $We = 45.27$, we observe complete coalescence with a tendency for a jet formation at the bottom surface of the crater. As we increase D_r , we expect to see complete coalescence at even higher We values but at $D_r = 1.25$, we surprisingly notice that complete coalescence starts at a lower We of 11.32 compared to $We = 20.02$ in case of $D_r = 1$. The cascading process for the $D_r = 1.25$ starts off by producing a single satellite at $We = 0.03$, increasing to three satellites at $We = 0.11$. The number of satellites produced reduces again to one for higher We and remains constant till the start of complete coalescence at $We = 11.32$. For $D_r = 1.5$, the whole range of We spans through partial coalescence except for an intermediate value of $We = 20.02$. Here too, we see a single satellite formation at the start, followed by the formation of two satellites at $We = 0.11$, and the number of satellites produced gets reduced again as We is increased. For higher D_r values, the regime of complete coalescence completely vanishes, and partial coalescence of various stages of cascade prevails throughout the $We - D_r$ space. From the regime map, we can see that the top-left portion represents the regions of complete coalescence suggesting that lower diameter ratios and higher Weber numbers may lead to complete coalescence. However, the number of satellites produced throughout this $We - D_r$ space varies arbitrarily, indi-

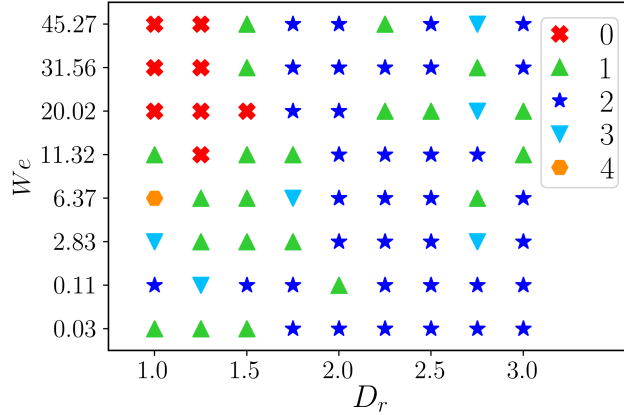


Figure 14: Regime map demarcating the complete and partial coalescence behaviours in We and D_r space for conglomerate-pool interaction. The numbers in the legend represent the stages of the cascade. The red-crosses corresponding to zero stages of cascade represent complete coalescence.

cating the strong influence of the shape of the conglomerate and the complex interaction of capillary waves in determining the overall coalescence behaviour.

5. Conclusions

The present study enables one to understand the coalescence dynamics of an arbitrary-shaped liquid conglomerate with a pool at a low impact velocity. The investigation is conducted through numerical simulations using an in-house flow solver. The effect of the diameter ratio (D_r) and the Weber number (We) on the coalescence dynamics is examined by keeping the size of the mother drop fixed. For a low value of Weber number ($We = 0.11$), we observe a transition from complete to partial coalescence for two interacting drops as D_r increases. However, the liquid conglomerate exhibits a partial coalescence behaviour with the pool for all the values of D_r investigated. The influence of the pool on the coalescence dynamics of the two drops is also quantified. We demonstrate that even though the extent to which the apex of the mother drop is stretched during its coalescence with the father drop is nearly the same for the cases with and without the presence of the pool, satellite generation is inhibited for cases where

the pool is too close to the father drop. The time duration for the bottom-most point of the father drop to reach from its initial position to a position at the onset of coalescence of the conglomerate with the pool (τ_r) is influenced by the movement of the capillary waves generated during the interaction between the father and mother drops. The pinch-off time (τ_p) for the first satellite drop increases consistently with an increase in D_r when the conglomerate and pool are considered. The pinch-off time for the first satellite drop becomes minimal for $D_r = 1$. This is explained in the context of an interplay between the shape of the conglomerate and the complex interaction of the capillary waves. A new morphology has also been observed during the pinch-off of the first satellite drop for $D_r = 1$. The morphology looks different from the columnar structure usually observed during a normal pinch-off. The variation of the ratio of the size of the satellite to that of the conglomerate (D_s/D_c) with D_r is studied. It is found that decreasing the value of D_r increases the value of D_s/D_c . The previously measured parameters (τ_p and D_s/D_c) for the conglomerate-pool interaction are then compared to the cases involving purely spherical drops, and the deviations are reported. Additionally, the dynamics of a falling drop that is initiated with the shape of the conglomerate is compared to that of the conglomerate. We observe that, in contrast to drops coalescing over superhydrophobic surfaces, the coalesced conglomerate retains the memory of its origin. Finally, a regime map on a $We - D_r$ space is constructed, which demarcates the complete and partial coalescence regions for the conglomerate-pool interaction. The arbitrary variation in the number of satellites produced throughout this $We - D_r$ space shows the influence of the shape of the conglomerate and complex trajectories of capillary waves in dictating the general coalescence process. Hence, the current investigation opens up the scope of further studies unravelling the effect of drop shape in coalescence dynamics.

6. Acknowledgements:

G.B. acknowledges his gratitude to J. C. Bose National Fellowship of SERB, Government of India (JBR/ 2021/ 000042). K.C.S. thanks the Science & Engineering Research Board, India for the financial support through grant CRG/2020/000507.

References

- Ajaev, V.S., Kabov, O.A., 2021. Levitation and self-organization of droplets. *Annu. Rev. Fluid Mech* 53, 203–225.
- Anna, S.L., 2016. Droplets and bubbles in microfluidic devices. *Annu. Rev. Fluid Mech.* 48, 285–309.
- Barea, J.S., Lee, J., Kang, D.K., 2019. Recent advances in droplet-based microfluidic technologies for biochemistry and molecular biology. *Micromachines* 10, 412.
- Benther, J.D., Pelaez-Restrepo, J.D., Stanley, C., Rosengarten, G., 2021. Heat transfer during multiple droplet impingement and spray cooling: Review and prospects for enhanced surfaces. *Int. J. Heat Mass Transf.* 178, 121587.
- Biswas, G., Ray, B., Sharma, A., 2011. Effect of drop shape on partial coalescence, in: *Russian-Indian Workshop on Topical Problems of Solid and Fluid Mechanics*, Repino (Russian Federation), July 1-5.
- Blanchette, F., Bigioni, T.P., 2006. Partial coalescence of drops at liquid interfaces. *Nat. Phys.* 2, 254–257.
- Brackbill, J.U., Kothe, D.B., Zemach, C., 1992. A continuum method for modeling surface tension. *J. Comput. Phys.* 100, 335–354.
- Chan, D.Y.C., Klaseboer, E., Manica, R., 2011. Film drainage and coalescence between deformable drops and bubbles. *Soft Matt.* 7, 2235–2264.

- Chang, Y.C., Hou, T.Y., Merriman, B., Osher, S., 1996. A level set formulation of Eulerian interface capturing methods for incompressible fluid flows. *J. Comput. Phys.* 124, 449–464.
- Charles, G.E., Mason, S.G., 1960. The mechanism of partial coalescence of liquid drops at liquid/liquid interfaces. *J. Colloid Sci.* 15, 105–122.
- Chen, X., Mandre, S., Feng, J.J., 2006. Partial coalescence between a drop and a liquid-liquid interface. *Phys. Fluids* 18, 051705.
- Cong, H., Qian, L., Wang, Y., Lin, J., 2020. Numerical simulation of the collision behaviors of binary unequal-sized droplets at high weber number. *Phys. Fluids* 32, 103307.
- Damak, M., Varanasi, K., 2018. Expansion and retraction dynamics in drop-on-drop impacts on nonwetting surfaces. *Phys. Rev. Fluids* 3, 093602.
- Davanlou, A., 2016. The role of liquid properties on lifetime of levitated droplets. *Langmuir* 32, 9736–9742.
- Deka, H., Biswas, G., Chakraborty, S.K., Dalal, A., 2019a. Coalescence dynamics of unequal sized drops. *Phys. Fluids* 31, 012105.
- Deka, H., Biswas, G., Sahu, K.C., Kulkarni, Y., Dalal, A., 2019b. Coalescence dynamics of a compound drop on a deep liquid pool. *J. Fluid Mech.* 866, R2.
- Gerlach, D., Tomar, G., Biswas, G., Durst, F., 2006. Comparison of volume-of-fluid methods for surface tension-dominant two-phase flows. *Int. J. Heat Mass Transfer* 49, 740–754.
- Gilet, T., Mulleners, K., Lecomte, J.P., Vandewalle, N. and Dorbolo, S., 2007a. Critical parameters for the partial coalescence of a droplet. *Phys. Rev. E* 75, 036303.
- Gilet, T., Vandewalle, N., Dorbolo, S., 2007b. Controlling the partial coalescence of a droplet on a vertically vibrated bath. *Phys. Rev. E.* 76, 035302.

- Harlow, F.H., Welch, J.E., 1965. Numerical calculation of time-dependent viscous incompressible flow of fluid with free surface. *Phys. Fluids* 8, 2182–2189.
- Hassanzadeh, M., Ahmadi Nadooshan, A., Bayareh, M., 2019. Numerical simulation of the head-on collision of two drops in a vertical channel. *J. of the Brazilian Soc. of Mechanical Sciences and Engineering* 41, 1–14.
- He, Z., Tran, H., Pack, M.Y., 2021. Drop bouncing dynamics on ultrathin films. *Langmuir* 37, 10135–10142.
- Honey, E.M., Kavehpour, H.P., 2006. Astonishing life of a coalescing drop on a free surface. *Phys. Rev. E* 73, 027301.
- Kavehpour, H.P., 2015. Coalescence of drops. *Annu. Rev. of Fluid Mech.* 47, 245–268.
- Kirar, P.K., Alvarenga, K., Kolhe, P.S., Biswas, G., Sahu, K.C., 2020. Coalescence of drops on the free-surface of a liquid pool at elevated temperatures. *Phys. Fluids* 32, 052103.
- Kirar, P.K., Kolhe, P.S., Sahu, K.C., 2022. Coalescence and migration of a droplet on a liquid pool with an inclined bottom wall. *Phys. Rev. Fluids* 7, 094001.
- Liu, Q., Lo, J.H.Y., Li, Y., Liu, Y., Zhao, J., Xu., L., 2021. The role of drop shape in impact and splash. *Nat. Commun.* 12, 3068.
- Markt Jr, D., Raessi, M., Lee, S.Y., Zhu, X., 2021. High-speed impact of micron-sized diesel drop trains—splashing dynamics, secondary droplet formation, and effects of pre-existing film thickness. *Phys. Fluids* 33, 102120.
- Paulsen, J.D., Carmigniani, R., Kannan, A., Burton, J.C., Nagel, S.R., 2014. Coalescence of bubbles and drops in an outer fluid. *Nat. Commun.* 5, 1–7.
- Poureslami, P., Faghiri, S., Shafii, M.B., 2023. Simultaneous double droplet impact on a molten phase change material pool: An experimental investigation. *Phys. Fluids* 35, 027110.

- Puckett, E.G., Almgren, A.S., Bell, J.B., Marcus, D.L., Rider, W.J., 1997. A high-order projection method for tracking fluid interfaces in variable density incompressible flows. *J. Comput. Phys.* 130, 269–282.
- Pumphrey, H.C., Crum, L.A., Bjørnø, L., 1989. Underwater sound produced by individual drop impacts and rainfall. *J. Acoust. Soc. Am.* 85, 1518–1526.
- Qian, J., Law, C.K., 1997. Regimes of coalescence and separation in droplet collision. *J. Fluid Mech.* 331, 59–80.
- Ray, B., Biswas, G., Sharma, A., 2010. Generation of secondary droplets in coalescence of a drop at a liquid–liquid interface. *J. Fluid Mech.* 655, 72–104.
- Ray, B., Biswas, G., Sharma, A., Welch, S.W.J., 2013. CLSVOF method to study consecutive drop impact on liquid pool. *Int. J. Numer. Methods Heat Fluid Flow* 23, 143–158.
- Reynolds, O., 1881. On the floating of drops on the surface of water depending only on the purity of the surface. *Proc. Lit. Phil. Soc. Manchester* 21, 413–414.
- Rider, W.J., Kothe, D.B., 1998. Reconstructing volume tracking. *J. Comput. Phys.* 141, 112–152.
- Rudman, M., 1997. Volume-tracking methods for interfacial flow calculations. *Int. J. Numer. Methods Fluids* 24, 671–691.
- Saha, A., Wei, Y., Tang, X., Law, C.K., 2019. Kinematics of vortex ring generated by a drop upon impacting a liquid pool. *J. Fluid Mech.* 875, 842–853.
- Shahriari, A., Ozkan, O., Bahadur, V., 2017. Electrostatic suppression of the leidenfrost state on liquid substrates. *Langmuir* 33, 13207–13213.
- Shen, Y., Xu, J., Yang, M., Huang, Y., Zhang, C., Zhou, J., Sun, K., Meng, S., 2022. Durably self-sustained droplet on a fully miscible liquid film. *Langmuir* 38, 3993–4000.

- Singh, S., Saha, A.K., 2022. Dynamics of two unequal-sized drops coalescence at a liquid-liquid interface. *Phys. Fluids* 34, 063604.
- Son, G., 2003. Efficient implementation of a coupled level-set and volume-of-fluid method for three-dimensional incompressible two-phase flows. *Numerical Heat Transfer: Part B: Fundamentals* 43, 549–565.
- Son, G., Hur, N., 2002. A coupled level set and volume-of-fluid method for the buoyancy-driven motion of fluid particles. *Numerical Heat Transfer: Part B: Fundamentals* 42, 523–542.
- Sprittles, J.E., Shikhmurzaev, Y.D., 2012. Coalescence of liquid drops: Different models versus experiment. *Phys. Fluids* 24, 122105.
- Stone, H.A., Stroock, A.D., Ajdari, A., 2004. Engineering flows in small devices: microfluidics toward a lab-on-a-chip. *Annu. Rev. Fluid Mech.* 36, 381–411.
- Sun, K., Zhang, P., Law, C.K., Wang, T., 2015. Collision dynamics and internal mixing of droplets of non-newtonian liquids. *Phys. Rev. Appl.* 4, 054013.
- Sussman, M., Puckett, E.G., 2000. A coupled level set and volume-of-fluid method for computing 3D and axisymmetric incompressible two-phase flows. *J. Comput. Phys.* 162, 301–337.
- Tang, C., Zhang, P., Law, C.K., 2012. Bouncing, coalescence, and separation in head-on collision of unequal-size droplets. *Phys. Fluids* 24, 022101.
- Tang, X., Saha, A., Law, C.K., Sun, C., 2016. Nonmonotonic response of drop impacting on liquid film: mechanism and scaling. *Soft Matter* 12, 4521–4529.
- Tang, X., Saha, A., Law, C.K., Sun, C., 2019. Bouncing drop on liquid film: Dynamics of interfacial gas layer. *Phys. Fluids* 31, 013304.
- Thomson, J.J., Newall, H.F., 1886. On the formation of vortex rings by drops falling into liquids, and some allied phenomena. *Proc. Royal Soc. Lond.* 39, 417–436.

- Thoroddsen, S.T., Etoh, T.G., Takehara, K., 2008. High-speed imaging of drops and bubbles. *Annu. Rev. Fluid Mech.* 40, 257–285.
- Thoroddsen, S.T., Takehara, K., 2000. The coalescence cascade of a drop. *Phys. Fluids* 12, 1265–1267.
- Thoroddsen, S.T., Takehara, K., Etoh, T.G., 2005. The coalescence speed of a pendent and a sessile drop. *J. Fluid Mech.* 527, 85–114.
- Thrivikraman, N.P., Khare, A., Hegde, A.S., Harikrishnan, A.R., 2021. Confined evaporation-mediated enhanced residence time of levitated water drops over deep oil pools. *Langmuir* 37, 14472–14482.
- Yi, N., Huang, B., Dong, L., Quan, X., Hong, F., Tao, P., Song, C., Shang, W., Deng, T., 2014. Temperature-induced coalescence of colliding binary droplets on superhydrophobic surface. *Sci. Rep.* 4, 1–5.
- Yoon, Y., Baldessari, F., Cenicerros, H.D., Leal, L.G., 2007. Coalescence of two equal-sized deformable drops in an axisymmetric flow. *Phys. Fluids* 19, 102102.
- Zhang, F.H., Li, E.Q., Thoroddsen, S.T., 2009. Satellite formation during coalescence of unequal size drops. *Phys. Rev. Lett.* 102, 104502.